

New relativistic effective interaction for finite nuclei, infinite nuclear matter and neutron stars

Bharat Kumar^{1,2}, B. K. Agrawal^{2,3}, and S. K. Patra^{1,2}

¹*Institute of Physics, Bhubaneswar-751005, India*

²*Homi Bhabha National Institute, Training School Complex, Anushakti Nagar, Mumbai 400085, India and*

³*Saha Institute of Nuclear Physics, 1/AF, Bidhannagar, Kolkata - 700064, India.*

(Dated: June 11, 2022)

We carry out the study for finite nuclei, infinite nuclear matter and neutron star properties with the newly developed relativistic force named as the Institute Of Physics Bhubaneswar-I(IOPB-I). Using this force, we calculate the binding energies, charge radii and neutron skin thickness for some selected nuclei. From the ground state properties of superheavy element *i.e.* $Z=120$, it is noticed that considerable shell gaps appear at neutron numbers $N=172, 184$ and 198 , showing the magicity of these numbers. The low density behavior of the equation of state for pure neutron matter is compatible with other microscopic models. Along with the nuclear symmetry energy, its slope and curvature parameters at the saturation density are consistent with those extracted from various experimental data. We calculate the neutron star properties with the equation of state composed of nucleons and leptons in *beta-equilibrium* which are in good agreement with the X-ray observations by Steiner and Nättilä. We find that the maximum mass of the neutron star to be $2.15M_{\odot}$ and stellar radius 11.936 km. Moreover, the radius and tidal deformability of a *canonical* neutron star mass $1.4M_{\odot}$ come out to be 13.242 km and $3.910 \times 10^{36} \text{ g cm}^2 \text{ s}^2$ respectively within this parameter set.

PACS numbers: 26.60.+c, 26.60.Kp, 95.85.Sz

I. INTRODUCTION

In the present scenario nuclear physics and nuclear astrophysics are well described within the self-consistent effective mean field models [1]. These effective theories are not only successful to describe the properties of finite nuclei but also explain nicely the nuclear matter systems at highly densified region [2]. The beauty of the effective models is that the nuclear system can be described by both relativistic as well as non-relativistic frame work within acceptable range. In recent decades, using the relativistic and non-relativistic formalisms, a large number of nuclear phenomena have been predicted near the nuclear drip-lines [3–5]. As a results, several experiments are planed in various laboratories to probe more deeper side of the unknown nuclear territories, *i.e.*, the neutron and proton drip-lines. Among the effective theories, the relativistic mean field (RMF) model is one of the most successful self-consistent formalism, which is currently drew attention for theoretical studies of such systems.

Although, the method of construction of the energy density functional in RMF formalism is different than the non-relativistic models, such as Skyrme [6, 7] and Gogny interactions [8], the obtained results for finite nuclei are in general, almost similar with one another. The same accuracy in prediction is also valid for the properties of the neutron stars.

In principle, the relativistic mean field (RMF) formalism is one step ahead than the non-relativistic one [9]. This is because, at higher density, the relativistic effects are more prominent which are taken care within the frame-work. Although, quantum chromodynamics(QCD) is the theory for strong interaction, the degrees of freedom in the RMF formalism are the nucleons and mesons, which is one step more fundamental than the non-relativistic theories. These mesons are responsible for the various nuclear properties and collectively taken as effective fields and denoted by classical numbers, which are the quantum mechanical expectation values.

In brief, one can say that the RMF formalism is the relativistic Hartree or Hartree Fock approximations of the one boson exchange (OBE) theory of nuclear interactions. In OBE theory, the nucleons interact through each other by exchange of isovector π -, ρ - and δ -mesons and isoscalar like η -, ρ - and ω - mesons. The π - and η -mesons are pseudo-scalar in nature and do not obey the ground state parity symmetry. In mean field level, they do not have contribution to the nuclear ground state properties.

The first and simple successful Lagrangian is formed by taking only the σ -, ω - and ρ - mesons contribution into account without any non-linear term to the Lagrangian density. This model predicts an unphysical large incompressibility K of ~ 600 MeV for infinite nuclear matter at saturation [9]. In order to lower the value of K to an acceptable range, the self-coupling terms in sigma meson are included by Boguta and Bodmer [10]. Based on this Lagrangian density, a large number of parameter sets, such as NL1 [11], NL2 [11], NL-SH [12], NL3 [13] and NL3* [14] are designed. The addition of σ -meson self-couplings improved the quality of finite nuclei properties and incompressibility remarkably, however it could not reproduce the equation of states upto satisfaction. Thus, the addition of vector meson self-coupling is introduced into the Lagrangian density and different parameter sets are constructed [15–17]. These sets are able to explain the finite nuclei and nuclear matter properties to a great extend, but till some shortcomings are there to explain the Coester-band problem as well as the 3-body interaction force. Subsequently, the nuclear physicists also change their way of thinking and introduced different strategies to improve the result by designing the density dependent coupling constants and effective field theory motivated relativistic mean field (E-RMF) model [1, 18].

Further, motivated by the effective field theory, Furnstahl *et. al.* [1] used all possible couplings upto 4^{th} order of expansion, constraining the nive dimensional analysis (NDA)

and naturalness, constructed the G1 and G2 parameter sets. In the Lagrangian density, they some how ignored the contribution of the mixed coupling isovector-isoscalar coupling, which has a greater implication on neutron radius and equation of state of asymmetric nuclear matter [19]. Later on it is also realized that the contribution of δ -meson is also needed to explain certain properties of nuclear phenomena in extreme conditions [20, 21]. The contribution of the δ -meson to bulk properties is nominal in normal nuclear matter, but for highly asymmetric nuclear matter as well as finite nuclei, it's effect is significance, mostly at high density. This meson, splits the effective masses of proton and neutron, which influences the production of $K^{+,-}$ and π^{+}/π^{-} in the heavy ion collision (HIC) [22]. Also, it increases the proton fraction in β -stable matter and modifies the transport properties of neutron star and heavy ion reaction [23–25]. The source terms for both the ρ - and δ -mesons contain isospin density, but their origin are different. The ρ -meson arises from the asymmetry in the number density and the evolution of the δ -meson is from the mass asymmetry of the nucleons.

Because of their different in origin, there are certain physical observables like neutron skin thickness, isotopic shift, two neutron separation energy S_{2n} , symmetry energy $S(\rho)$, giant dipole resonance (GDR) and effective mass of the nucleons, which are correlated with the isovector channel of the system will be influenced, if one ignores the effects of δ -meson. From the observation of skin data for Sn isotopes, it is clear that, the skin thickness is marginally affected by the shell closer, but significantly from the contribution of the symmetry energy. The symmetry energy has a strong correlation with the neutron-skin, but till now experiments have not fixed the accurate value of neutron radius, which are under consideration for verification in the parity violating electron nucleus scattering experiments [18, 26].

Recently, the detection of gravitational waves from binary neutron star GW170817 is a major breakthrough in astrophysics which is detected for the first time by the advanced Laser Interferometer Gravitational wave (aLIGO) and advanced VIRGO detectors [27]. This detection has certainly posed to be a valuable guidance to study matter under the most extreme conditions. Inspiral and coalescing objects of a binary neutron star result in gravitational waves. Due to the merger, a compact remnant is remaining whose nature is decided by two factors *i.e* (i) the masses of the inspiralling objects and (ii) the equation of state of the neutron star matter. For final state, the formation of either a neutron star or a black hole depend on the masses and stability of the objects. The chirp mass is measured very precisely from data analysis of GW170817 and it is found to be $1.188^{+0.004}_{-0.002} M_{\odot}$ for the 90% credible intervals. It is suggested that total mass should be $2.74^{+0.04}_{-0.01} M_{\odot}$ for low-spin priors and $2.82^{+0.47}_{-0.09} M_{\odot}$ for high-spin priors [27]. Moreover, the maximum mass of nonspinning neutron stars (NSs) as a function of radius are observed with the highly precise measurements of $M \approx 2M_{\odot}$. From the observations of gravitational waves, we can extract information

regarding the radii or tidal deformability of the nonspinning and spinning NSs [28–30]. Once succeed in getting this information, it is easy to get the neutron star matter equation of state [31, 32].

In this paper, we constructed a new parameter set IOPB-I using the simulate annealing method (SAM) [33–35] and explore the generic prediction of properties of finite nuclei, nuclear matter and neutron stars within the E-RMF formalism. Our new parameter set is confronted the considerable shell gap appears at neutron numbers $N=172, 184$ and 198 showing the magicity of these numbers. The behavior of the density dependent symmetry energy of nuclear matter at low and high density are examined in detail. The effect of the core EoS on the mass, radius and tidal deformability of a NS are evaluated using the static $l = 2$ perturbation of a Tolman-Oppenheimer-Volkoff solution.

The paper is organized as follows: In Sec. II, we outline the effective field theory motivated relativistic mean field (E-RMF) Lagrangian. We derived the equations of motion for finite nuclei and equation of states (EoS) for infinite nuclear matter. In Sec. III, we discussed the strategy of the parameter fitting using the simulated annealing method (SAM). After getting the new parameter sets IOPB-I, the results on binding energy, two neutron separation energy, neutron-skin thickness for finite nuclei are discussed in Sec. IVA. In Sec. IVB and IVC, the EoS for symmetric and asymmetric matters are presented. The mass-radius and tidal deformability of the neutron star obtained by this new set are also discussed in this section. Finally, the summary and concluding remarks are given in Sec. V.

Conventions: We have taken the value of $G = c = 1$ through the manuscript.

II. FORMALISM

A. Energy density functional and equations of motion

In this section, we outline briefly the E-RMF Lagrangian [1]. The beauty of effective Lagrangian is that, one can ignore the basic difficulties of the formalism, like renormalization and divergence of the system. The model can be used directly by fitting the coupling constants and some masses of the mesons. The E-RMF Lagrangian has an infinite number of terms with all type of self and cross couplings. It is necessary to develop a truncation procedure for practical use. Generally, the meson fields constructed in the Lagrangian are smaller than the mass of the nucleon. Their ratio could be used as an truncation scheme as it is done in Refs. [1, 3, 36, 37] along with the NDA and naturalness properties. The basic nucleon-meson E-RMF Lagrangian (with δ -meson, $W \times R$) is upto 4th order with exchange mesons like σ -, ω -, ρ -meson and photon A is given as [1, 38]:

$$\begin{aligned}
\mathcal{E}(r) = & \sum_{\alpha} \varphi_{\alpha}^{\dagger}(r) \left\{ -i\boldsymbol{\alpha} \cdot \boldsymbol{\nabla} + \beta [M - \Phi(r) - \tau_3 D(r)] + W(r) + \frac{1}{2} \tau_3 R(r) + \frac{1 + \tau_3}{2} A(r) \right. \\
& - \frac{i\beta\boldsymbol{\alpha}}{2M} \cdot \left(f_{\omega} \boldsymbol{\nabla} W(r) + \frac{1}{2} f_{\rho} \tau_3 \boldsymbol{\nabla} R(r) \right) \left. \right\} \varphi_{\alpha}(r) + \left(\frac{1}{2} + \frac{\kappa_3}{3!} \frac{\Phi(r)}{M} + \frac{\kappa_4}{4!} \frac{\Phi^2(r)}{M^2} \right) \frac{m_s^2}{g_s^2} \Phi^2(r) \\
& - \frac{\zeta_0}{4!} \frac{1}{g_{\omega}^2} W^4(r) + \frac{1}{2g_s^2} \left(1 + \alpha_1 \frac{\Phi(r)}{M} \right) (\boldsymbol{\nabla} \Phi(r))^2 - \frac{1}{2g_{\omega}^2} \left(1 + \alpha_2 \frac{\Phi(r)}{M} \right) \\
& (\boldsymbol{\nabla} W(r))^2 - \frac{1}{2} \left(1 + \eta_1 \frac{\Phi(r)}{M} + \frac{\eta_2}{2} \frac{\Phi^2(r)}{M^2} \right) \frac{m_{\omega}^2}{g_{\omega}^2} W^2(r) - \frac{1}{2e^2} (\boldsymbol{\nabla} A(r))^2 - \frac{1}{2g_{\rho}^2} (\boldsymbol{\nabla} R(r))^2 \\
& - \frac{1}{2} \left(1 + \eta_{\rho} \frac{\Phi(r)}{M} \right) \frac{m_{\rho}^2}{g_{\rho}^2} R^2(r) - \Lambda_{\omega} (R^2(r) \times W^2(r)) + \frac{1}{2g_{\delta}^2} (\boldsymbol{\nabla} D(r))^2 + \frac{1}{2} \frac{m_{\delta}^2}{g_{\delta}^2} (D^2(r)) , \quad (1)
\end{aligned}$$

where Φ , W , R , D and A are the fields, σ , g_{ω} , g_{ρ} , g_{δ} , $\frac{e^2}{4\pi}$ are the coupling constants and m_{σ} , m_{ω} , m_{ρ} and m_{δ} are the masses for σ , ω , ρ , δ mesons and photon, respectively.

Now, our aim is to solve the field equations for the baryons

and mesons (nucleon, σ , ω , ρ , δ) using the variational principle defined as $\left(\frac{\partial \mathcal{E}}{\partial \phi_i} \right)_{\rho=\text{constant}} = 0$. The Dirac equation corresponds to the energy density eqn. (1) becomes

$$\begin{aligned}
& \left\{ -i\boldsymbol{\alpha} \cdot \boldsymbol{\nabla} + \beta [M - \Phi(r) - \tau_3 D(r)] + W(r) + \frac{1}{2} \tau_3 R(r) + \frac{1 + \tau_3}{2} A(r) \right. \\
& \left. - \frac{i\beta\boldsymbol{\alpha}}{2M} \cdot \left[f_{\omega} \boldsymbol{\nabla} W(r) + \frac{1}{2} f_{\rho} \tau_3 \boldsymbol{\nabla} R(r) \right] \right\} \varphi_{\alpha}(r) = \varepsilon_{\alpha} \varphi_{\alpha}(r) . \quad (2)
\end{aligned}$$

The mean field equations for Φ , W , R , D and A are given by

$$\begin{aligned}
-\Delta\Phi(r) + m_s^2\Phi(r) &= g_s^2\rho_s(r) - \frac{m_s^2}{M}\Phi^2(r)\left(\frac{\kappa_3}{2} + \frac{\kappa_4}{3!}\frac{\Phi(r)}{M}\right) \\
&+ \frac{g_s^2}{2M}\left(\eta_1 + \eta_2\frac{\Phi(r)}{M}\right)\frac{m_\omega^2}{g_\omega^2}W^2(r) + \frac{\eta_\rho}{2M}\frac{g_s^2}{g_\rho^2}m_\rho^2R^2(r) \\
&+ \frac{\alpha_1}{2M}[(\nabla\Phi(r))^2 + 2\Phi(r)\Delta\Phi(r)] + \frac{\alpha_2}{2M}\frac{g_s^2}{g_\omega^2}(\nabla W(r))^2, \tag{3}
\end{aligned}$$

$$\begin{aligned}
-\Delta W(r) + m_\omega^2W(r) &= g_\omega^2\left(\rho(r) + \frac{f_\omega}{2}\rho_T(r)\right) - \left(\eta_1 + \frac{\eta_2}{2}\frac{\Phi(r)}{M}\right)\frac{\Phi(r)}{M}m_\omega^2W(r) \\
&- \frac{1}{3!}\zeta_0W^3(r) + \frac{\alpha_2}{M}[\nabla\Phi(r) \cdot \nabla W(r) + \Phi(r)\Delta W(r)] \\
&- 2\Lambda_\omega g_\omega^2R^2(r)W(r), \tag{4}
\end{aligned}$$

$$-\Delta R(r) + m_\rho^2R(r) = \frac{1}{2}g_\rho^2\left(\rho_3(r) + \frac{1}{2}f_\rho\rho_{T,3}(r)\right) - \eta_\rho\frac{\Phi(r)}{M}m_\rho^2R(r) - 2\Lambda_\omega g_\rho^2R(r)W^2(r), \tag{5}$$

$$-\Delta A(r) = e^2\rho_p(r), \tag{6}$$

$$-\Delta D(r) + m_\delta^2D(r) = g_\delta^2\rho_{s3}, \tag{7}$$

where the baryon, scalar, isovector, proton and tensor densities are

$$\begin{aligned}
\rho(r) &= \sum_\alpha \varphi_\alpha^\dagger(r)\varphi_\alpha(r), \\
&= \rho_p(r) + \rho_n(r) \\
&= \frac{2}{(2\pi)^3} \int_0^{k_p} d^3k + \frac{2}{(2\pi)^3} \int_0^{k_n} d^3k. \tag{8}
\end{aligned}$$

$$\begin{aligned}
\rho_s(r) &= \sum_\alpha \varphi_\alpha^\dagger(r)\beta\varphi_\alpha(r), \\
&= \rho_{sp}(r) + \rho_{sn}(r) \\
&= \sum_\alpha \frac{2}{(2\pi)^3} \int_0^{k_\alpha} d^3k \frac{M_\alpha^*}{(k_\alpha^2 + M_\alpha^{*2})^{\frac{1}{2}}}, \tag{9}
\end{aligned}$$

$$\begin{aligned}
\rho_3(r) &= \sum_\alpha \varphi_\alpha^\dagger(r)\tau_3\varphi_\alpha(r), \\
&= \rho_p(r) - \rho_n(r) \tag{10}
\end{aligned}$$

$$\begin{aligned}
\rho_{s3}(r) &= \sum_\alpha \varphi_\alpha^\dagger(r)\tau_3\beta\varphi_\alpha(r), \\
&= \rho_{ps}(r) - \rho_{ns}(r) \tag{11}
\end{aligned}$$

$$\rho_p(r) = \sum_\alpha \varphi_\alpha^\dagger(r)\left(\frac{1+\tau_3}{2}\right)\varphi_\alpha(r), \tag{12}$$

$$\rho_T(r) = \sum_\alpha \frac{i}{M}\nabla \cdot [\varphi_\alpha^\dagger(r)\beta\alpha\varphi_\alpha(r)], \tag{13}$$

$$\rho_{T,3}(r) = \sum_\alpha \frac{i}{M}\nabla \cdot [\varphi_\alpha^\dagger(r)\beta\alpha\tau_3\varphi_\alpha(r)], \tag{14}$$

where k_α is the nucleon's Fermi momentum. The effective mass of proton M_p^* and neutron M_n^* are written as

$$M_p^* = M - \Phi(r) - D(r), \tag{15}$$

$$M_n^* = M - \Phi(r) + D(r), \tag{16}$$

The vector potential is

$$V(r) = g_\omega V_0(r) + \frac{1}{2}g_\rho\tau_3b_0(r) + e\frac{(1-\tau_3)}{2}A_0(r). \tag{17}$$

The set of coupled differential equations are solved self-consistently to describe the ground state properties of finite nuclei. In the fitting procedure, we used the experimental data of binding energy (BE) and charge radius r_{ch} for a set of spherical nuclei (^{16}O , ^{40}Ca , ^{48}Ca , ^{68}Ni , ^{90}Zr , $^{100,132}\text{Sn}$ and ^{208}Pb). The total binding energy is obtained by summing the individual contribution, which is given by:

$$\begin{aligned}
E_{total} &= E_{part} + E_\sigma + E_\omega + E_\rho \\
&+ E_\delta + E_{\omega\rho} + E_c + E_{pair} + E_{c.m.}, \tag{18}
\end{aligned}$$

where E_{part} is the sum of the single particle energies of the nucleons and E_σ , E_ω , E_ρ , E_δ , E_c are the contribution of the

respective mesons and Coulomb fields. The pairing E_{pair} and the centre of mass motion $E_{cm} = \frac{3}{4}.41A^{-1/3}$ MeV energies are also taken into account [3, 39, 40]. The BCS pairing with the addition of few quasi-particle states are used to take care of the nucleon pairing near the Fermi surface [3].

B. Nuclear Matter Properties

1. Energy and pressure density

In a static, infinite, uniform and isotropic nuclear matter, all

the gradients of the fields in Eqs.(3)-(7) vanish. By the definition of infinite nuclear matter, the electromagnetic interaction is also neglected. The expressions for energy density and pressure for such a system is obtained from the energy-momentum tensor [41]:

$$T_{\mu\nu} = \sum_i \partial_\nu \phi_i \frac{\partial \mathcal{L}}{\partial (\partial^\mu \phi_i)} - g_{\mu\nu} \mathcal{L}. \quad (19)$$

The zeroth component of the energy-momentum tensor $< T_{00} >$ gives the energy density and the third component $< T_{ii} >$ compute the pressure of the system [38]:

$$\begin{aligned} \mathcal{E} = & \frac{2}{(2\pi)^3} \int d^3k E_i^*(k) + \rho W + \frac{m_s^2 \Phi^2}{g_s^2} \left(\frac{1}{2} + \frac{\kappa_3}{3!} \frac{\Phi}{M} + \frac{\kappa_4}{4!} \frac{\Phi^2}{M^2} \right) \\ & - \frac{1}{2} m_\omega^2 \frac{W^2}{g_\omega^2} \left(1 + \eta_1 \frac{\Phi}{M} + \frac{\eta_2}{2} \frac{\Phi^2}{M^2} \right) - \frac{1}{4!} \frac{\zeta_0 W^4}{g_\omega^2} + \frac{1}{2} \rho_3 R \\ & - \frac{1}{2} \left(1 + \frac{\eta_\rho \Phi}{M} \right) \frac{m_\rho^2}{g_\rho^2} R^2 - \Lambda_\omega (R^2 \times W^2) + \frac{1}{2} \frac{m_\delta^2}{g_\delta^2} (D^2), \end{aligned} \quad (20)$$

$$\begin{aligned} P = & \frac{2}{3(2\pi)^3} \int d^3k \frac{k^2}{E_i^*(k)} - \frac{m_s^2 \Phi^2}{g_s^2} \left(\frac{1}{2} + \frac{\kappa_3}{3!} \frac{\Phi}{M} + \frac{\kappa_4}{4!} \frac{\Phi^2}{M^2} \right) \\ & + \frac{1}{2} m_\omega^2 \frac{W^2}{g_\omega^2} \left(1 + \eta_1 \frac{\Phi}{M} + \frac{\eta_2}{2} \frac{\Phi^2}{M^2} \right) + \frac{1}{4!} \frac{\zeta_0 W^4}{g_\omega^2} \\ & + \frac{1}{2} \left(1 + \frac{\eta_\rho \Phi}{M} \right) \frac{m_\rho^2}{g_\rho^2} R^2 + \Lambda_\omega (R^2 \times W^2) - \frac{1}{2} \frac{m_\delta^2}{g_\delta^2} (D^2), \end{aligned} \quad (21)$$

where $E_i^*(k) = \sqrt{k^2 + M_i^{*2}}$ ($i = p, n$) is the energy and k is the momentum of the nucleon. In the context of density functional theory, it is possible to parametrize the exchange and correlation effects through local potentials (Kohn-Sham potentials), as long as those contributions be small enough [42]. The Hartree values control the dynamics in the relativistic Dirac-Brückner-Hartree-Fock (DBHF) calculations. Therefore, the local meson fields in the RMF formalism can be interpreted as Kohn-Sham potentials and in this sense equations (2-7) include effects beyond the Hartree approach through the non-linear couplings [1].

2. Symmetry Energy

The binding energy per nucleon $\mathcal{E}/A = e(\rho, \alpha)$ can be written in the parabolic form of asymmetry parameter

$$\alpha \left(= \frac{\rho_n - \rho_p}{\rho_n + \rho_p} \right):$$

$$e(\rho, \alpha) = \frac{\mathcal{E}}{\rho_B} - M = e(\rho) + S(\rho) \alpha^2 + \mathcal{O}(\alpha^4), \quad (22)$$

where $e(\rho)$ is energy density of the symmetric nuclear matter (SNM) ($\alpha = 0$) and $S(\rho)$ is defined as the symmetry energy of the system:

$$S(\rho) = \frac{1}{2} \left[\frac{\partial^2 e(\rho, \alpha)}{\partial \alpha^2} \right]_{\alpha=0}. \quad (23)$$

The isospin asymmetry arises due to the difference in densities and masses of the neutron and proton. The density type isospin asymmetry is taken care by ρ -meson (isovector-vector meson) and mass asymmetry by δ -meson (isovector -

scalar meson). The general expression for symmetry energy $S(\rho)$ is a combine expression of ρ - and δ -mesons, which is defined as [3, 20, 43, 44]:

$$S(\rho) = S^{kin}(\rho) + S^\rho(\rho) + S^\delta(\rho), \quad (24)$$

with

$$S^{kin}(\rho) = \frac{k_F^2}{6E_F^*}; \quad S^\rho(\rho) = \frac{g_\rho^2 \rho}{8m_\rho^{*2}} \quad (25)$$

and

$$S^\delta(\rho) = -\frac{1}{2}\rho \frac{g_\delta^2}{m_\delta^2} \left(\frac{M^*}{E_F} \right)^2 u_\delta(\rho, M^*). \quad (26)$$

The last function u_δ is from the discreteness of the Fermi momentum. This momentum is quite large in nuclear matter and can be treated as a continuum and continuous system. The function u_δ is defined as:

$$u_\delta(\rho, M^*) = \frac{1}{1 + 3 \frac{g_\delta^2}{m_\delta^2} \left(\frac{\rho^s}{M^*} - \frac{\rho}{E_F} \right)}. \quad (27)$$

In the limit of continuum, the function $u_\delta \approx 1$. The whole symmetry energy ($S^{kin} + S^{pot}$) arises from ρ - and δ -mesons is given as:

$$S(\rho) = \frac{k_F^2}{6E_F^*} + \frac{g_\rho^2 \rho}{8m_\rho^{*2}} - \frac{1}{2}\rho \frac{g_\delta^2}{m_\delta^2} \left(\frac{M^*}{E_F} \right)^2, \quad (28)$$

where E_F^* is the Fermi energy and k_F is the Fermi momentum. The mass of the ρ -meson modified, because of the cross-coupling of $\rho - \omega$ fields and is given by

$$m_\rho^{*2} = \left(1 + \eta_\rho \frac{\Phi}{M} \right) m_\rho^2 + 2g_\rho^2(\Lambda_\omega W^2). \quad (29)$$

The cross-coupling of isoscalar-isovector mesons (Λ_ω) modified the density dependent of $S(\rho)$ without affecting the saturation properties of the symmetric nuclear matter (SNM) [26, 45, 46]. In the numerical calculation, the coefficient of symmetry energy $S(\rho)$ is obtained by the energy difference of symmetric and pure neutron matter at saturation. In our calculation, we have taken the isovector channel into account to make the new parameter, which incorporates the current existing experimental observation and prediction be done for some future aspect of the model. The symmetry energy can be expanded in a Taylor series around the saturation density ρ_0 as:

$$S(\rho) = J + L\mathcal{Y} + \frac{1}{2}K_{sym}\mathcal{Y}^2 + \frac{1}{6}Q_{sym}\mathcal{Y}^3 + \mathcal{O}[\mathcal{Y}^4], \quad (30)$$

where $J = S(\rho_0)$ is the symmetry energy at saturation and $\mathcal{Y} = \frac{\rho - \rho_0}{3\rho_0}$. The coefficients $L(\rho_0)$ and $K_{sym}(\rho_0)$ are defined as:

$$L = 3\rho \frac{\partial S(\rho)}{\partial \rho} \Big|_{\rho=\rho_0}, \quad (31)$$

$$K_{sym} = 9\rho^2 \frac{\partial^2 S(\rho)}{\partial \rho^2} \Big|_{\rho=\rho_0=0}, \quad (32)$$

$$Q_{sym} = 27\rho^3 \frac{\partial^3 S(\rho)}{\partial \rho^3} \Big|_{\rho=\rho_0=0}. \quad (33)$$

Similarly, we can obtain the asymmetric nuclear matter (ANM) incompressibility as $K(\alpha) = K + K_\tau \alpha^2 + \mathcal{O}(\alpha^4)$ and K_τ is given by [47]

$$K_\tau = K_{sym} - 6L - \frac{Q_0 L}{K}, \quad (34)$$

where $Q_0 = 27\rho^3 \frac{\partial^3 (\mathcal{E}/\rho)}{\partial \rho^3}$ in SNM.

Here, L is the slope and K_{sym} represents the curvature of $S(\rho)$ at saturation density. A large number of investigations have been made to fix the value of J , L and K_{sym} [45, 48–53]. The density dependence of symmetry energy is a key quantity to control the properties of both finite nuclei and infinite nuclear matter [54]. Currently, the available information on symmetry energy $J = 31.6 \pm 2.66$ MeV and its slope $L = 58.9 \pm 16$ MeV at saturation density are obtained by various astrophysical observations [55]. Since, till date, it does not have a precise value and also the experimental data of neutron radius of some nuclei so far measured accumulate a large error, therefore it is essential to discuss the behavior of the symmetry energy as a function of density in our new parameter set.

III. PARAMETER FITTING

The simulated annealing method (SAM) is used to determine the parameters used in the Lagrangian density [56, 57]. The SAM is useful in the global minimization technique, *i.e.*, it gives accurate results when there exist a global minimum within several local minima. Usually, this procedure is used in a system when the number of parameters are more than the observables [58–60]. In this simulation method, the system stabilizes, when the temperature T (a variable which controls the energy of the system) goes down. Initially, the nuclear system is put at a high temperature (highly unstable) and then allowed to cool down slowly so that it is stabilized in a very smooth way and finally reaches the frozen temperature (stable or systematic system). The variation of T should be very small near the stable state. The $\chi^2 = \chi^2(p_1, \dots, p_N)$ values of the considered systems are minimized (least-square fit), which is governed by the model parameters p_i . The general expression of the χ^2 can be given as:

$$\chi^2 = \frac{1}{N_d - N_p} \sum_{i=1}^{N_d} \left(\frac{M_i^{exp} - M_i^{th}}{\sigma_i} \right)^2. \quad (35)$$

Here, N_d and N_p are the numbers of the experimental data points and the fitting parameters, respectively. The experimental and theoretical values are given by M_i^{exp} and M_i^{th} , respectively. The σ_i are theoretical errors in the measurements.

For proper working of the SAM technique, first one should fix the schedule and appropriate parameter spacing (acceptable range of parameters) in which χ^2 -minimization to be taken. The schedule is fixed by Cauchy annealing formulae which is given as:

$$T(k) = \frac{T_i}{k+1}, \quad (36)$$

where T_i is the initial control parameter (also known as temperature of the system) and $T(k)$ is the control parameter after completing the k^{th} step. The value of k is increased by unity after completing 100 N_p , 10 N_p successful reconfigurations, whichever occurs first. In the present parameter calculations, we used the methodology of the earlier works of Refs. [21, 33–35].

In our present calculations, we have built a new parameter set IOPB-I and analyzed their effects for finite and infinite nuclear systems. Thus, we performed an overall fit with 13 parameters, where the nucleons as well as the masses of the two vector mesons in free space are fixed at their experimental values *i.e.*, $M = 939$ MeV, $m_\omega = 782.5$ MeV and $m_\rho = 763.0$ MeV. The effective mass can be used as a nuclear matter constraint at the saturation density ρ_0 along with other empirical values like incompressibility, binding energy per nucleon and asymmetric parameter J . While fitting the parameter, the value of effective mass M^*/M , nuclear matter incompressibility K and symmetry energy coefficient J are constrained within 0.50-0.90, 220-260 MeV and 28-36 MeV respectively. The calculated results of the binding energy and charge radius compared with the known experimental data. Finally, the minimum χ^2 is obtained by simulated annealing method to fix the final parameters. The newly developed IOPB-I set along with NL3 [13], FSUGarnet [61] and G3 [21] are given for comparison in Table I. It is to be noted that in the original E-RMF parametrization, only five spherical nuclei are taken into consideration while fitting the parameters with the binding energy, charge radius and single particle energy [1]. Here, eight spherical nuclei are used for the job as listed in Table II.

IV. RESULTS AND DISCUSSIONS

In this section we discuss our calculated results for finite nuclei and infinite nuclear matter. For finite nuclei, the binding energy, neutron and proton radii, two neutron separation energy etc. are analyzed. Similarly, for infinite nuclear matter system, the binding energy per particle for symmetric and asymmetric nuclear matter including pure neutron matter at both sub-saturation and supra-saturation are compared with other theoretical results and experimental data. The parameter set is also applied to study the structure of neutron star using β -equilibrium and charge neutrality conditions.

A. FINITE NUCLEI

(i) Binding energies, charge radii and neutron-skin thickness

TABLE I: The obtained new parameter set IOPB-I along with NL3 [13], FSUGarnet [61] and G3 [21] sets are listed. The nucleon mass M is 939.0 MeV. All the coupling constants are dimensionless, except k_3 which is in fm^{-1} .

	NL3	FSUGarnet	G3	IOPB-I
m_s/M	0.541	0.529	0.559	0.533
m_ω/M	0.833	0.833	0.832	0.833
m_ρ/M	0.812	0.812	0.820	0.812
m_δ/M	0.0	0.0	1.043	0.0
$g_s/4\pi$	0.813	0.837	0.782	0.827
$g_\omega/4\pi$	1.024	1.091	0.923	1.062
$g_\rho/4\pi$	0.712	1.105	0.962	0.885
$g_\delta/4\pi$	0.0	0.0	0.160	0.0
k_3	1.465	1.368	2.606	1.496
k_4	-5.688	-1.397	1.694	-2.932
ζ_0	0.0	4.410	1.010	3.103
η_1	0.0	0.0	0.424	0.0
η_2	0.0	0.0	0.114	0.0
η_ρ	0.0	0.0	0.645	0.0
Λ_ω	0.0	0.043	0.038	0.024
α_1	0.0	0.0	2.000	0.0
α_2	0.0	0.0	-1.468	0.0
$f_\omega/4$	0.0	0.0	0.220	0.0
$f_\rho/4$	0.0	0.0	1.239	0.0
β_σ	0.0	0.0	-0.087	0.0
β_ω	0.0	0.0	-0.484	0.0

We used eight spherical nuclei to fit the experimental ground-state binding energy and charge radii using SAM. The calculated results are listed in Table II and compared with other theoretical models as well as experimental data [62, 63]. It can be seen that the NL3 [13], FSUGarnet [61] and G3 [21] successfully reproduce the energies and charge radii as well. Although, the “mean field models are not well qualified for light nuclei” and marginally reproduce experimental ground state properties [64], we noticed that both the binding energy and charge radius of ^{16}O are well produced by IOPB-I. However, the charge radii of $^{40,48}\text{Ca}$ are slightly underestimate the data. We would like to emphasize that it is an open challenge to mean field models to predict the evolution of charge radii for $^{38-52}\text{Ca}$ (see Fig. 3 in Ref. [65]).

The excess of neutrons gives rise to a neutron-skin thickness (NST) in the neutron rich nuclei. It is distinguished by the neutron distribution extending the proton distribution, *i. e.* the difference between the neutron and proton rms radii and is defined as,

$$\Delta r_{np} = \langle r^2 \rangle_n^{1/2} - \langle r^2 \rangle_p^{1/2} = R_n - R_p. \quad (37)$$

In atomic nuclei, NST is a perfect signal of isovector property and it is correlated with the slope of the symmetry energy [66–68]. In Fig. 1, we show NST Δr_{np} for ^{40}Ca to ^{238}U nuclei as a function of proton-neutron asymmetry $I = (N - Z)/A$.

TABLE II: The calculated binding energy per particle (B/A) and charge radius (R_c) are compared with the available experimental data [62, 63]. The predicted neutron-skin thickness $\Delta r_{np} = R_n - R_p$ is also depicted with all the four models.

Nucleus	Obs.	Expt.	NL3	FSUGarnet	G3	IOPB-I
^{16}O	B/A	7.976	7.917	7.876	8.037	7.977
	R_c	2.699	2.714	2.690	2.707	2.705
	$R_n - R_p$	-	-0.026	-0.028	-0.028	-0.027
^{40}Ca	B/A	8.551	8.540	8.528	8.561	8.577
	R_c	3.478	3.466	3.438	3.459	3.458
	$R_n - R_p$	-	-0.046	-0.051	-0.049	-0.049
^{48}Ca	B/A	8.666	8.636	8.609	8.671	8.638
	R_c	3.477	3.443	3.426	3.466	3.446
	$R_n - R_p$	-	0.229	0.169	0.174	0.202
^{68}Ni	B/A	8.682	8.698	8.692	8.690	8.707
	R_c	-	3.870	3.861	3.892	3.873
	$R_n - R_p$	-	0.262	0.184	0.190	0.223
^{90}Zr	B/A	8.709	8.695	8.693	8.699	8.691
	R_c	4.269	4.253	4.231	4.276	4.253
	$R_n - R_p$	-	0.115	0.065	0.068	0.091
^{100}Sn	B/A	8.258	8.301	8.298	8.266	8.284
	R_c	-	4.469	4.426	4.497	4.464
	$R_n - R_p$	-	-0.073	-0.078	-0.079	-0.077
^{132}Sn	B/A	8.355	8.371	8.372	8.359	8.352
	R_c	4.709	4.697	4.687	4.732	4.706
	$R_n - R_p$	-	0.349	0.224	0.243	0.287
^{208}Pb	B/A	7.867	7.885	7.902	7.863	7.870
	R_c	5.501	5.509	5.496	5.541	5.521
	$R_n - R_p$	-	0.283	0.162	0.180	0.221

TABLE III: The nuclear matter properties such as binding energy per nucleon \mathcal{E}_0 (MeV), saturation density ρ_0 (fm^{-3}), incompressibility coefficient for symmetric nuclear matter K (MeV), effective mass ratio M^*/M , symmetry energy J (MeV) and linear density dependence of the symmetry energy L (MeV) at saturation.

	NL3	FSUGarnet	G3	IOPB-I
ρ_0 (fm^{-3})	0.148	0.153	0.148	0.149
\mathcal{E}_0 (MeV)	-16.29	-16.23	-16.02	-16.10
M^*/M	0.595	0.578	0.699	0.593
J (MeV)	37.43	30.95	31.84	33.30
L (MeV)	118.65	51.04	49.31	63.58
K_{sym} (MeV)	101.34	59.36	-106.07	-37.09
Q_{sym} (MeV)	177.90	130.93	915.47	862.70
K (MeV)	271.38	229.5	243.96	222.65
Q_0	211.94	15.76	-466.61	-101.37
K_τ	-703.23	-250.41	-307.65	-389.46
K_{asy}	-610.56	-246.89	-401.97	-418.58
K_{sat2}	-703.23	-250.41	-307.65	-389.46

The calculated results of Δr_{np} for NL3, FSUGarnet, G3 and IOPB-I parameter sets are compared with the corresponding experimental data [69]. Experiments have been done with antiprotons at CERN and extracted data of the NST of 26 stable nuclei ranging from ^{40}Ca to ^{238}U displayed in the figure with the error bars. The trend on the data points show approximately linear dependence of NST on the relative neutron

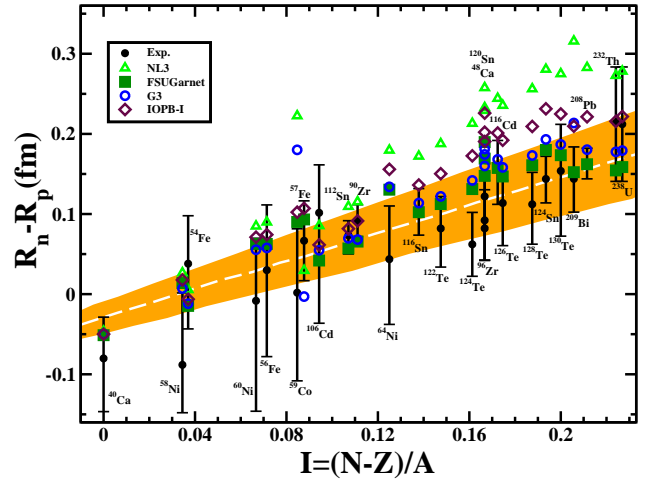


FIG. 1: (color online) The neutron skin thickness as a function of the asymmetry parameter. Results obtained with the parameter set IOPB-I are compared with those of the set NL3 [13], FSUGarnet [61], G3 [21] and experimental values [69]. The shaded region is calculated using Eq.38.

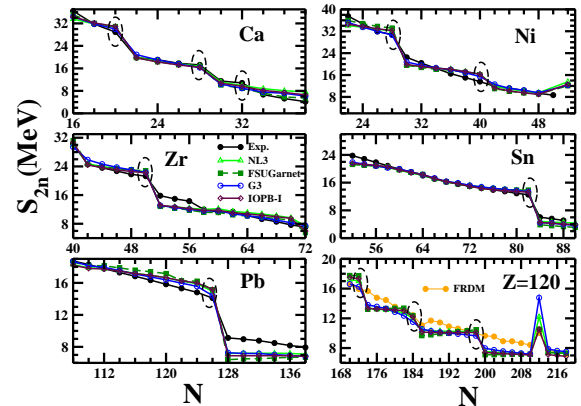


FIG. 2: (color online) The two-neutron separation energy as a function of neutron number for the isotopic series of Ca, Ni, Zr, Sn and Pb nuclei with NL3 [13], FSUGarnet [61], G3 [21], FRDM [70] and experimental data [62] whenever available. The dotted circle represents the magicity of the nuclei.

TABLE IV: The binary neutron star masses ($m_1(M_\odot), m_2(M_\odot)$) and corresponding radii ($R_1(\text{km}), R_2(\text{km})$), tidal love number ($(k_2)_1, (k_2)_2$), tidal deformabilities (λ_1, λ_2) and dimensionless tidal deformabilities (Λ_1, Λ_2). $\tilde{\Lambda}, \delta\tilde{\Lambda}, \mathcal{M}_c(M_\odot)$ and $\mathcal{R}_c(\text{km})$ are the dimensionless tidal deformability, tidal correction, chirp mass and radius of the binary neutron star, respectively.

EoS	$m_1(M_\odot)$	$m_2(M_\odot)$	$R_1(\text{km})$	$R_2(\text{km})$	$(k_2)_1$	$(k_2)_2$	λ_1	λ_2	Λ_1	Λ_2	$\tilde{\Lambda}$	$\delta\tilde{\Lambda}$	$\mathcal{M}_c(M_\odot)$	$\mathcal{R}_c(\text{km})$
NL3	1.20	1.20	14.702	14.702	0.1139	0.1139	7.826	7.826	2983.15	2983.15	2983.15	0.000	1.04	10.350
	1.50	1.20	14.736	14.702	0.0991	0.1139	6.889	7.826	854.06	2983.15	1608.40	220.223	1.17	10.214
	1.25	1.25	14.708	14.708	0.1118	0.1118	7.962	7.962	2388.82	2388.82	2388.82	0.000	1.09	10.313
	1.30	1.30	14.714	14.714	0.1094	0.1094	7.546	7.546	1923.71	1923.71	1923.71	0.000	1.13	10.271
	1.35	1.35	14.720	14.720	0.1070	0.1070	7.393	7.393	1556.84	1556.84	1556.84	0.000	1.18	10.224
	1.35	1.25	14.720	14.708	0.1070	0.1118	7.393	7.962	1556.84	2388.82	1930.02	91.752	1.13	10.268
	1.37	1.25	14.722	14.708	0.1061	0.1118	7.339	7.962	1452.81	2388.82	1863.78	100.532	1.14	10.271
	1.40	1.20	14.726	14.702	0.1044	0.1139	7.231	7.826	1267.07	2983.15	1950.08	183.662	1.13	10.262
	1.40	1.40	14.726	14.726	0.1044	0.1044	7.231	7.231	1267.07	1267.07	1267.07	0.000	1.22	10.174
	1.42	1.29	14.728	14.712	0.1031	0.1099	7.147	7.572	1145.72	1994.02	1515.18	95.968	1.18	10.192
	1.44	1.39	14.730	14.724	0.1027	0.1049	7.120	7.259	1108.00	1311.00	1204.83	19.212	1.23	10.179
	1.45	1.45	14.732	14.732	0.1018	0.1018	7.064	7.064	1037.13	1037.13	1037.13	0.000	1.26	10.124
	1.54	1.26	14.740	14.708	0.0969	0.1114	6.741	7.668	729.95	2303.95	1308.91	168.202	1.21	10.179
	1.60	1.60	14.746	14.746	0.0937	0.0937	6.532	6.532	589.92	589.92	589.92	0.000	1.39	9.979
FSUGarnet	1.20	1.20	12.944	12.944	0.1090	0.1090	3.961	3.961	1469.32	1469.32	1469.32	0.000	1.04	8.983
	1.50	1.20	12.972	12.944	0.0893	0.1090	3.282	3.961	408.91	1469.32	784.09	111.643	1.17	8.847
	1.25	1.25	12.958	12.958	0.1062	0.1062	3.880	3.880	1193.78	1193.78	1193.78	0.000	1.09	8.977
	1.30	1.30	12.968	12.968	0.1030	0.1030	3.777	3.777	945.29	945.29	945.29	0.000	1.13	8.910
	1.35	1.35	12.974	12.974	0.0998	0.0998	3.666	3.666	761.13	761.13	761.13	0.000	1.18	8.860
	1.35	1.25	12.974	12.958	0.0998	0.1062	3.666	3.880	761.13	1193.78	955.00	49.744	1.13	8.920
	1.37	1.25	12.976	12.958	0.0986	0.1062	3.629	3.880	710.62	1193.78	922.54	53.853	1.14	8.924
	1.40	1.20	12.978	12.944	0.0965	0.1090	3.552	3.961	622.06	1469.32	959.22	90.970	1.13	8.904
	1.40	1.40	12.978	12.978	0.0965	0.0965	3.552	3.552	622.06	622.06	622.06	0.000	1.22	8.825
	1.42	1.29	12.978	12.966	0.0949	0.1038	3.495	3.803	565.47	1001.18	755.10	50.492	1.18	8.867
	1.44	1.39	12.978	12.978	0.0939	0.0973	3.456	3.582	531.54	653.60	589.65	14.148	1.23	8.823
	1.45	1.45	12.978	12.978	0.0931	0.0931	3.427	3.427	507.70	507.70	507.70	0.000	1.26	8.776
	1.54	1.26	12.964	12.960	0.0862	0.1057	3.157	3.864	343.73	1146.73	638.35	88.892	1.21	8.817
	1.60	1.60	12.944	12.944	0.0816	0.0816	2.964	2.964	266.20	266.20	266.20	0.000	1.39	8.511
G3	1.20	1.20	12.466	12.466	0.1034	0.1034	3.114	3.114	1776.65	1776.65	1776.65	0.000	1.04	9.331
	1.50	1.20	112.360	12.466	0.0800	0.1034	2.309	3.114	284.92	1776.65	803.43	191.605	1.17	8.890
	1.25	1.25	12.460	12.460	0.1001	0.1001	3.007	3.007	939.79	939.79	939.79	0.000	1.09	8.557
	1.30	1.30	12.448	12.448	0.0962	0.0962	2.875	2.875	728.07	728.07	728.07	0.000	1.13	8.457
	1.35	1.35	12.434	12.434	0.0925	0.0925	2.750	2.750	582.26	582.26	582.26	0.000	1.18	8.398
	1.35	1.25	12.434	12.460	0.0925	0.1001	2.750	3.007	582.26	939.79	742.29	43.064	1.13	8.482
	1.37	1.25	12.428	12.460	0.0909	0.1001	2.696	3.007	530.66	939.79	709.72	49.144	1.14	8.468
	1.40	1.20	12.416	12.466	0.0859	0.1034	2.613	3.114	461.03	1776.65	976.80	183.274	1.13	8.937
	1.40	1.40	12.416	12.416	0.0859	0.0859	2.613	2.613	461.03	461.03	461.03	0.000	1.22	8.312
	1.42	1.29	12.408	12.450	0.0868	0.0972	2.553	2.905	417.96	772.17	571.87	43.226	1.18	8.387
	1.44	1.39	12.398	12.420	0.0854	0.0894	2.501	2.643	384.42	484.90	432.22	12.671	1.23	8.292
	1.45	1.45	12.932	12.392	0.0846	0.0846	2.472	2.472	367.04	367.04	367.04	0.000	1.26	8.225
	1.54	1.26	12.334	12.458	0.0769	0.0992	2.194	2.976	239.49	883.46	474.83	75.175	1.21	8.311
	1.60	1.60	12.280	12.280	0.0716	0.0716	2.000	2.000	179.63	179.63	179.63	0.000	1.39	7.867

TABLE V: Table IV is continued ...

EoS	$m_1(M_\odot)$	$m_2(M_\odot)$	$R_1(\text{km})$	$R_2(\text{km})$	$(k_2)_1$	$(k_2)_2$	λ_1	λ_2	Λ_1	Λ_2	$\tilde{\Lambda}$	$\delta\tilde{\Lambda}$	$\mathcal{M}_c(M_\odot)$	$\mathcal{R}_c(\text{km})$
IOPB-I	1.20	1.20	13.222	13.222	0.1081	0.1081	4.369	4.369	1654.23	1654.23	1654.23	0.000	1.04	9.199
	1.50	1.20	13.236	13.222	0.0894	0.1081	3.631	4.369	449.62	1654.23	875.35	128.596	1.17	9.044
	1.25	1.25	13.230	13.230	0.1053	0.1053	4.268	4.268	1310.64	1310.64	1310.64	0.000	1.09	9.146
	1.30	1.30	13.238	13.238	0.1024	0.1024	4.162	4.162	1053.07	1053.07	1053.07	0.000	1.13	9.105
	1.35	1.35	13.240	13.240	0.0995	0.0995	4.050	4.050	857.53	857.53	857.53	0.000	1.18	9.074
	1.35	1.25	13.240	13.230	0.0995	0.1053	4.050	4.268	857.53	1310.64	1060.81	49.565	1.13	9.110
	1.37	1.25	13.242	13.230	0.0938	0.1053	4.004	4.268	791.92	1310.64	1019.60	56.371	1.14	9.104
	1.40	1.20	13.242	13.222	0.0960	0.1081	3.911	4.369	680.79	1654.23	1067.64	107.340	1.13	9.097
	1.40	1.40	13.242	13.242	0.0960	0.0960	3.911	3.911	680.79	680.79	680.79	0.000	1.22	8.986
	1.42	1.29	13.242	13.236	0.0949	0.1030	3.864	4.184	632.31	1099.78	835.91	52.836	1.18	9.049
	1.44	1.39	13.242	13.242	0.0935	0.0969	3.806	3.946	578.47	719.80	645.73	17.094	1.23	8.985
	1.45	1.45	13.240	13.240	0.0927	0.0927	3.771	3.771	549.06	549.06	549.06	0.000	1.26	8.915
	1.54	1.26	13.230	13.232	0.0868	0.1047	3.516	4.247	384.65	1253.00	703.58	94.735	1.21	8.991
	1.60	1.60	13.212	12.212	0.0823	0.0823	3.314	3.314	296.81	296.81	296.81	0.000	1.39	8.698

excess I of nucleus that can be fitted by [69, 71]:

$$\Delta r_{np} = (0.90 \pm 0.15)I + (-0.03 \pm 0.02) \text{ fm}. \quad (38)$$

Some of the Δr_{np} obtained with IOPB-I slightly deviate from the shaded region and results of G3 and FSUGarnet lie inside it. This is because, IOPB-I has a smaller strength of $\omega - \rho$ cross-coupling as compared to G3 and FSUGarnet. The calculated values of NST for the ^{208}Pb nucleus are 0.283, 0.162, 0.180 and 0.221 fm for the NL3, FSUGarnet, G3 and IOPB-I parameter sets respectively. The proton elastic scattering experiment has recently measured NST $\Delta r_{np} = 0.211^{+0.054}_{-0.063}$ fm for ^{208}Pb [72]. Within this error bar, the IOPB-I prediction of neutron skin is 0.221 fm in ^{208}Pb turns out to be reasonably good.

(ii) Two-neutron separation energy $S_{2n}(Z, N)$

The large shell gap in single particle energy levels is an indication of the magic number. This means greater stability comes on the magic nuclei, when the nucleons in the lower level has contrast large value of energy than that in higher level. This extra stability for a particular number can be evaluated from the sudden fall in the two neutron separation energy S_{2n} . The S_{2n} can be estimated by the difference in binding energies of two isotopes that is related to the ground-state nuclear binding energies $BE(Z, N)$, $BE(Z, N - 2)$ with the relation:

$$S_{2n}(Z, N) = BE(Z, N) - BE(Z, N - 2). \quad (39)$$

In Fig. 2, we display results for the S_{2n} energy as a function of neutron numbers for Ca, Ni, Zr, Sn, Pb and $Z=120$ isotopic chain. The calculated results are compared with the finite range droplet model (FRDM) [70] and latest experimental data [62]. From the figure, it is clear that how the magicity evolves as one moves from the valley of stability to the

drip-line. In all cases, the S_{2n} values decrease gradually with increase in neutron number. The experimental shell effect at neutron number $N = 20, 28(\text{Ca}), 28(\text{Ni}), 50(\text{Zr}), 82(\text{Sn})$ and $126(\text{Pb})$ are reasonably well reproduced by the four relativistic sets. The flat behavior of Ca isotopes in S_{2n} from $N=30$ to $N=32$ is recently confirmed with the mass measurement at TITAN/TRIUMF [73]. It is shown that ^{52}Ca is more bound by 1.74 MeV than ^{50}Ca . Figure 2 shows that the experimental S_{2n} of $^{50-52}\text{Ca}$ are in good agreement with the prediction of NL3 set. It is interesting to note that all sets predict the sub-shell closure at $N=40$ for Ni isotopes.

Furthermore, the two-neutron separation energy for the isotopic series of nuclei $Z=120$ is also displayed in Fig. 2. With respect to the isotopic chain of $Z=120$, no experimental information exists. The only comparison can be made with theoretical model such as the FRDM [62]. At $N=172, 184$ and 198 sharp fall in separation energy can clearly be seen in all forces, which have been predicted by various theoretical models in superheavy mass region [74–77]. Therefore, a future mass measurement of $^{292,304,318}120$ would confirm a key test for theory, as well as direct information about the close-shell behavior at $N=172, 184$ and 198 .

B. Infinite Nuclear Matter System

The incompressibility K is defined the dynamical properties of the system, which shows that how much our system can be compressed at the saturation density ρ_0 without violating the Pauli exclusion principle. This plays as importance role in the nuclear equation of state (EoS). Currently, the accepted value of $K = 240 \pm 20$ MeV has been determined from isoscalar giant monopole resonance (ISGMR) for ^{90}Zr and ^{208}Pb nuclei [78, 79]. However, effective mean field model give around $200 - 300$ MeV [13, 21, 61]. In our param-

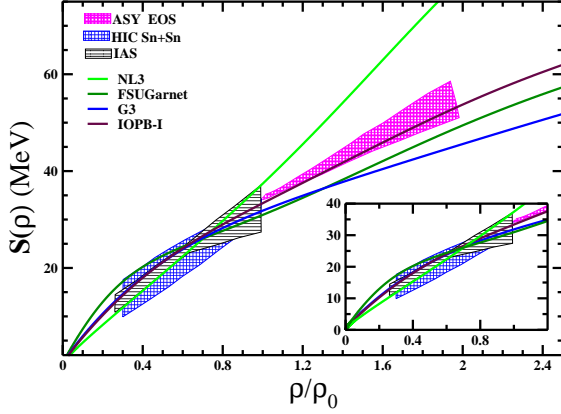


FIG. 3: (color online) Density dependent symmetry energy from Eq. (30) with different E-RMF parameter sets along with IOPB-I parametrization. The shaded region is the symmetry energy from IAS [80], HIC Sn+Sn [81] and ASY-EoS experimental data [82]. The zoomed pattern of the symmetry energy at low densities is shown in the inset.

ter fitting, we have found 222.65 MeV for constructing the coupling constant at the saturation density 0.149 fm^{-3} . The density dependent symmetry energy $S(\rho)$ is determined from Eq.(30) using IOPB-I along with three adopted models. The calculated results of the symmetry energy coefficient (J), the slope of symmetry energy (L) and other saturation properties are shown in Table III. Many studies have been devoted to search the strong correlations between the size of the neutron skin thickness of a neutron-rich heavy nucleus such as ^{208}Pb and the slope parameter (L) [44, 66, 83]. We find that IOPB-I gives $J = 33.30 \text{ MeV}$ and $L = 63.58 \text{ MeV}$. These values are compatible within the error bars of $J = 31.6 \pm 2.66 \text{ MeV}$ and $L = 58.9 \pm 16 \text{ MeV}$ obtained by various terrestrial experimental informations and astrophysical observations [55].

Another important constraint K_τ has been suggested from -840 MeV to -350 MeV [84–86] by various experiments on isoscalar giant monopole resonance, which we can calculate from Eq.(34). It is to be noticed that the calculated values of K_τ are -703.23, -250.41, -307.65 and -389.46 MeV for NL3, FSUGarnet, G3 and IOPB-I parameter set, respectively. The large value of K_τ for NL3 set comes from the larger nuclear matter incompressibility K and the absence of cross-couplings. Moreover, the ISGMR measurement has been investigated in a series of $^{112-124}\text{Sn}$ isotopes, which extracted the value of $K_\tau = -395 \pm 40 \text{ MeV}$ [87]. It is found that $K_\tau = -389.46 \text{ MeV}$ for IOPB-I set is also consistent with GMR measurement [87]. Since NL3 has a larger values of J and L , it yields larger NST (0.28 fm) for the ^{208}Pb nucleus. In the absence of cross-coupling, $S(\rho)$ of NL3 is stiffer at low and high density regime as displayed in Fig. 3. Alternatively, presence of cross-coupling of ρ mesons to the ω (in case of FSUGarnet and IOPB-I) and σ mesons (in case of G3) yields the softer symmetry energy at low density which are consistent with

HIC Sn+Sn [81], IAS [80] data as mentioned in the figure. However, IOPB-I has a less stiffer $S(\rho)$ comparison to NL3 parameter set at higher density which lies inside the shaded region of ASY-EoS experimental data [82].

Next, we display in Fig. 4 the binding energy per neutron (B/N) as a function of the neutron density. Here, special attention is needed to build nucleon-nucleon interaction to fit the data at sub-saturation density. For example, the EoS of pure neutron matter (PNM) at low density obtained within the variational method, which obtained with a Urbana v_{14} interaction [88]. In this regards, the effective mean field models are also fulfilled this demand to some extent [21, 61, 89]. The cross-coupling $\omega - \rho$ plays an important role at low-density of the PNM. The low-density (zoomed pattern) nature of the FSUGarnet, G3 and IOPB-I are in harmony with the results obtained by microscopic calculations [49, 88, 90–92]. While NL3 deviates from the shaded region at low as well as high densities regions. We also find a very good agreement for FSUGarnet, G3 and IOPB-I at higher densities, which have been obtained by microscopic calculations [49, 88, 90–92]. While NL3 deviates from the shaded region at low as well as high densities regions. We also find a very good agreement for FSUGarnet, G3 and IOPB-I at higher densities, which have been obtained by chiral NN and 3N interactions [93].

In Fig. 5, we show the calculated pressure P for the symmetric nuclear matter (SNM) and PNM with the baryon density for the four E-RMF models and results are compared with the experimental flow data [94]. It is seen from Fig. 5(a) that G3 parameter set is in excellent agreement in the entire density zone. The FSUGarnet and IOPB-I are stiffer in comparison with G3 set at higher densities $\approx (2.6 - 4.6)\rho_0$, which are also reliable with the experimental HIC data. In Fig. 5(b), the bounds on the PNM equation of states (EoSs) are divided into two categories (i) the upper one corresponds to a strong density dependence of symmetry energy $S(\rho)$ (HIC-Asy Stiff) and (ii) the lower one corresponds to the weakest $S(\rho)$ (HIC-Asy Soft) [94, 95]. Our parameter set IOPB-I along with G3 and FSUGarnet are reasonably good in agreement with experimental flow data. The PNM EoS for the IOPB-I model is quite stiffer than G3 at high densities.

C. Neutron stars

(i) Predicted equation of states

We have solved Eqs.(20-21) for the pressure and energy density of the *beta-equilibrated* charge neutral neutron star matter in which only baryon number and the charge number are conserved. The results display the pressure as a function of energy density for the IOPB-I along with NL3, FSUGarnet and G3 sets in Fig. 6. The solid circles are the central pressure and energy density corresponding to the maximum mass of the neutron star obtained from the above equations of state. The shaded region of the EoS can be divided into two parts as follows:

(i) Nättilä *et. al.* applied the Bayesian cooling tail method to constraint (1σ and 2σ confidenced limit) the EoS of cold densed matter inside the neutron stars [96].

(ii) Steiner *et. al.* have been determined an empirical densed matter EoS with 95% confidence limit from a heterogeneous data set containing PRE bursts and quiescent thermal emission from X-ray transients [97].

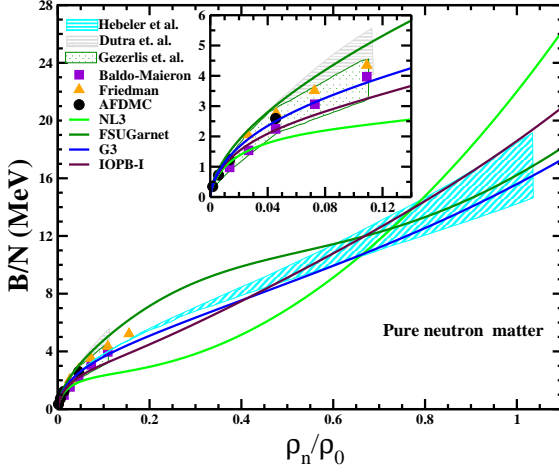


FIG. 4: (color online) The energy per neutron as a function of neutron density with NL3 [13], FSUGarnet [61], G3 [21] and IOPB-I parameter sets. Other curves and shaded region represents the results for various microscopic approaches such as Baldo-Maieron [90], Friedman [88], Auxiliary-field diffusion Monte Carlo [91], Dutra [49], Gezerlis [92] and Hebeler [93].

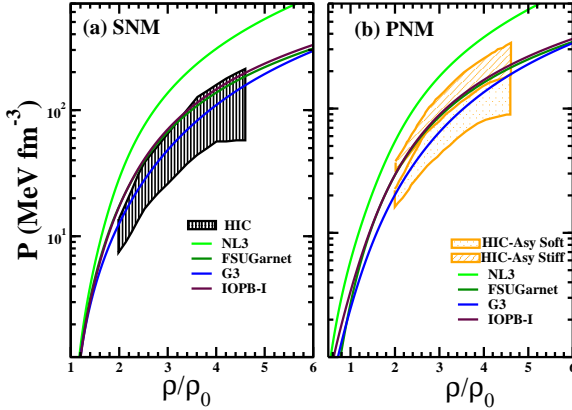


FIG. 5: (color online) Pressure as a function of baryon density for IOPB-I force. The results with NL3 [13], FSUGarnet [61], G3 [21] are compared with the EoS extracted from the analysis [94] for the (a) symmetric nuclear matter (SNM) and (b) pure neutron matter (PNM).

From Fig. 6, it is clear that IOPB-I and FSUGarnet EoSs are looking similar at high density but they differ remarkably at low densities as shown in the zoomed area of the inset. Note that among the EoSs, the celebrity NL3 set gives the stiffer EoS. Moreover, IOPB-I shows the stiffest EoS upto energy densities $\mathcal{E} \lesssim 700 \text{ MeV fm}^{-3}$. It can be seen that the results of IOPB-I at very high densities $\mathcal{E} \sim 400 - 1600 \text{ MeV fm}^{-3}$ consistent with the EoS obtained by Nättälä and Steiner *et al.* [96, 97]. But, FSUGarnet has a softer EoS at low energy densities $\mathcal{E} \lesssim 200 \text{ MeV fm}^{-3}$ and stiffer EoS at intermediate en-

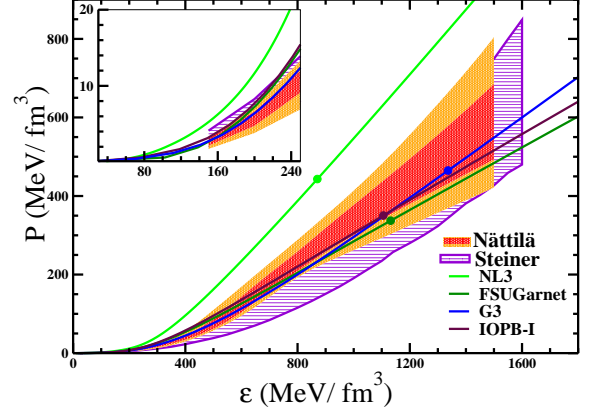


FIG. 6: (color online) The equations of states with NL3, FSUGarnet, G3 and IOPB-I for nuclear matter under charge neutrality as well as the β -equilibrium condition. The shaded region (violet) represents the observational constraint at $r_{ph} = R$ with uncertainty of 2σ [97]. Here, R and r_{ph} are the neutron star radius and the photospheric radius, respectively. Other shaded region (red+orange) represents the QMC+Model A equation of state of cold dense matter with 95% confidence limit [96]. The region zoomed near the origin is shown in the inset.

ergy densities compare to the relativistic energy density functional G3. One can notice that in Tables I and III, the softness in G3 [21] EoS is mainly due to the new couplings and not due to the difference in compressibility K as generally assumed. Remarkably the G3 set satisfies all the above mentioned constraints.

(ii) Mass-radius and tidal deformability of neutron star

After fixing the equation of state for the various parameter sets, we extend our study to calculate the mass, radius and tidal deformability of a non-rotating neutron star. Placing a spherical star in a static external quadrupolar tidal field \mathcal{E}_{ij} results in deformation of the star along with quadrupole deformation which is the leading order perturbation. Such a deformation is measured by

$$\lambda = -\frac{Q_{ij}}{\mathcal{E}_{ij}} = \frac{2}{3}k_2 R^5; \quad (40)$$

$$\Lambda = \frac{2k_2}{3C^5}. \quad (41)$$

Where Q_{ij} is the induced quadrupole moment of a star in binary, and \mathcal{E}_{ij} is the static external quadrupole tidal field of the companion star. λ is the tidal deformability parameter depending on the EoS via both the neutron star (NS) radius and a dimensionless quantity k_2 , called the second Love number [28, 30]. Λ is the dimensionless version of λ , and C is the compactness parameter ($C = M/R$). However, in general relativity (GR) we have to distinguish k_2 between gravitational fields generated by masses (electric-type) and those generated by the motion of masses, *i.e.* mass currents

(magnetic-type) [32, 99]. The electric tidal Love is found

from the following expression [30]:

$$k_2 = \frac{8}{5}(1-2C)^2 C^5 [2C(y-1) - y + 2] \left\{ 2C(4(y+1)C^4 + (6y-4)C^3 + (26-22y)C^2 + 3(5y-8)C - 3y + 6) - 3(1-2C)^2(2C(y-1) - y + 2) \log\left(\frac{1}{1-2C}\right) \right\}^{-1}. \quad (42)$$

The value of $y \equiv y(R)$ can be computed by solving the following first order differential equation [29, 32]:

$$r \frac{dy(r)}{dr} + y(r)^2 + y(r)F(r) + r^2 Q(r) = 0, \quad (43)$$

with,

$$F(r) = \frac{r - 4\pi r^3 [\mathcal{E}(r) - P(r)]}{r - 2M(r)}, \quad (44)$$

$$Q(r) = \frac{4\pi r(5\mathcal{E}(r) + 9P(r) + \frac{\mathcal{E}(r)+P(r)}{\partial P(r)/\partial \mathcal{E}(r)} - \frac{6}{4\pi r^2})}{r - 2M(r)} - 4 \left[\frac{M(r) + 4\pi r^3 P(r)}{r^2(1 - 2M(r)/r)} \right]^2. \quad (45)$$

To estimate the tidal deformability λ of a single star, Eq. (44) must be integrated simultaneously with Tolman-Oppenheimer-Volkov (TOV) equations [100], *i.e.*

$$\frac{dP(r)}{dr} = - \frac{[\mathcal{E}(r) + P(r)][M(r) + 4\pi r^3 P(r)]}{r^2(1 - \frac{2M(r)}{r})}, \quad (46)$$

and

$$\frac{dM(r)}{dr} = 4\pi r^2 \mathcal{E}(r). \quad (47)$$

For a given EoS and from the boundary conditions $P(0) = P_c$, $M(0)=0$, and $y(0) = 2$, where P_c , $M(0)$, and $y(0)$ are the central pressure, mass and dimensionless quantity. To obtain the tidal Love number, we solve this system of eqs. (40-47) for a given EoS of the star at $r=0$. The value of $r(=R)$ where the pressure vanishes define the surface of the star. Thus, at each central density we can uniquely determine a mass M , a radius R and tidal Love number k_2 of the isolated neutron star using the chosen EoSs. In Fig. 7, the horizontal bars in cyan and magenta include the results from the precisely measured neutron stars masses, such as PSR J1614-2230 with mass $M = 1.97 \pm 0.04 M_\odot$ [101] and PSR J0348+0432 ($M = 2.01 \pm 0.04 M_\odot$) [102]. We also depict the 1σ and 2σ empirical mass-radius constraints for the cold dense matter inside the NS which have been obtained from a Bayesian analysis of type-I X-ray burst observation [96]. Similar approach is applied by Steiner *et al.*, but they obtained the mass-radius from six sources, *i.e.*, three from transient low-mass X-ray binaries and three from type-I X-ray bursters with

photospheric radius [97]. Definitely, those observations revealed that the maximum mass predicted by any theoretical model should reach the limit $\sim 2.0 M_\odot$, which is consistent with all the equation of states for nucleonic matter as shown in Fig. 7.

The NL3 model of RMF theory suggests a larger and massive NS with mass $2.77 M_\odot$ and the corresponding NS radius to be 13.314 km, which is larger than the best observational radius estimates [96, 97]. Hence it is clear that the new E-RMF have been developed either through density-dependent couplings [44] or higher order couplings [21, 61]. These models successfully reproduce the ground-state properties of finite nuclei, nuclear matter saturation properties and also for the maximum mass of the neutron stars. Another important advantage of these models is that they are consistent with the sub-saturation density of the pure neutron matter. L. Rezzolla *et al.* [103] have combined the recent gravitational-wave observation of merging system of binary neutron stars via the event GW170817 with quasi-universal relations between the maximum mass of rotating and non-rotating NSs. It is found that the maximum mass for non-rotating NS should be in the range $2.01 \pm 0.04 \lesssim M(M_\odot) \lesssim 2.16 \pm 0.03$ [103], where the lower limit is observed from massive pulsars in binary system [102]. From the results we find that the maximum masses of IOPB-I along with FSUGarnet and G3 EoSs are consistent with the above boundary. The parametrization of the IOPB-I set, we find that the maximum mass of the NS is $2.15 M_\odot$ and the radius (without including crust) of the *canonical* mass is 13.242 km which is relatively larger as compared to the current X-ray observations radii of range 10.5-12.8 km by Nättilä *et al.* [96] and 11-12 km by Steiner *et al.* [97]. Similarly, FSUGarnet fails to qualify radius constraint. However, recently E. Annala *et al.* suggest that the radius of a $1.4 M_\odot$ star should be in the range $11.1 \leq R_{1.4 M_\odot} \leq 13.4$ km [98], which is consistent with the IOPB-I and FSUGarnet sets. Furthermore, G3 EoS is relatively softer at energy density $\mathcal{E} \gtrsim 200$ MeV fm $^{-3}$ (see in Fig. 6), which is able to reproduce the recent observational maximum mass of $2.0 M_\odot$ as well as the radius of the *canonical* neutron star mass of 12.416 km.

Now we move to another important calculation regarding the tidal deformability of the single neutron star as well as binary neutron stars (BNS) which has been recently discussed in GW170817 [27]. Eq. (41) indicates that λ strongly depends on the radius of the NS as well as on the value of k_2 . Moreover, k_2 depends on the internal structure of the constituent body and directly enters into the gravitational wave phase of

inspiralling BNS which in turn conveys information about the EoS. As the radii of the NS increases, the deformation by the external field becomes large as there will be increase in gravitational gradient with simultaneous increase in radius. As a consequence of this, a fixed mass of NS with large radius will be a stiff EoS and we get larger deformation in the BNS system. Whereas for smaller radii it will be a softer EoS and the deformation will be very small in these systems.

Fig. 8 shows the tidal deformability as a function of NS mass. In particular, λ takes a wide range of values $\lambda \sim (1-8) \times 10^{36} \text{ g cm}^2 \text{ s}^2$ as shown in Fig. 8. In the G3 parameter set, the tidal deformability λ is very low in the mass region $0.5 - 2.0 M_\odot$ in comparison with other sets. This is because the star exerts high central pressure and energy density resulting the formation of a compact star which is shown as solid dots in Fig. 6. However, in the NL3 EoS case, it turns out that, because of the stiffness of the EoS, the λ value is increasing. The tidal deformability of the canonical NS ($1.4 M_\odot$) of IOPB-I along with FSUGarnet and G3 EoSs are found to be 3.191, 3.552, and 2.613 $\text{g cm}^2 \text{ s}^2$, respectively as shown in Tables IV and V, which are consistent with the results obtained by Steiner *et al.* [104].

Next, we discuss the weighted dimensionless tidal deformability of the BNS of mass m_1 and m_2 and is defined as [27, 105, 106]:

$$\tilde{\Lambda} = \frac{8}{13} \left[(1 + 7\eta - 31\eta^2)(\Lambda_1 + \Lambda_2) + \sqrt{1 - 4\eta}(1 + 9\eta - 11\eta^2)(\Lambda_1 - \Lambda_2) \right], \quad (48)$$

with tidal correction

$$\delta\tilde{\Lambda} = \frac{1}{2} \left[\sqrt{1 - 4\eta} \left(1 - \frac{13272}{1319}\eta + \frac{8944}{1319}\eta^2 \right) (\Lambda_1 + \Lambda_2) + \left(1 - \frac{15910}{1319}\eta + \frac{32850}{1319}\eta^2 + \frac{3380}{1319}\eta^3 \right) (\Lambda_1 - \Lambda_2) \right]. \quad (49)$$

Here, $\eta = m_1 m_2 / M^2$ is the symmetric mass ratio, m_1 and m_2 are the binary masses, $M = m_1 + m_2$ is the total mass, Λ_1 and Λ_2 are the dimensionless tidal deformability of BNS, for the case $m_1 \geq m_2$. Also, we have taken equal and unequal-masses (m_1 and m_2) BNS system as it has been done in Refs. [109, 110]. The calculated results for the Λ_1 , Λ_2 and weighted tidal deformability $\tilde{\Lambda}$ of the present EoSs are displayed in Tables IV and V. In Fig. 9, we display the different dimensionless tidal deformabilities corresponding to a progenitor masses of the NS. It can be seen that the IOPB-I along with FSUGarnet and G3 are good agreement with the 90% and 50% probability contour of GW170817 [27]. Recently, aLIGO/VIRGO detectors have measured the value of $\tilde{\Lambda}$ whose results are more precise than the results found by considering the individual value of Λ_1 and Λ_2 of the BNS [27]. It is noticed that the value of $\tilde{\Lambda} \leq 800$ in the low-spin case and $\tilde{\Lambda} \leq 700$ in the high spin case within the 90% credible intervals which are consistent with the 680.79, 622.06

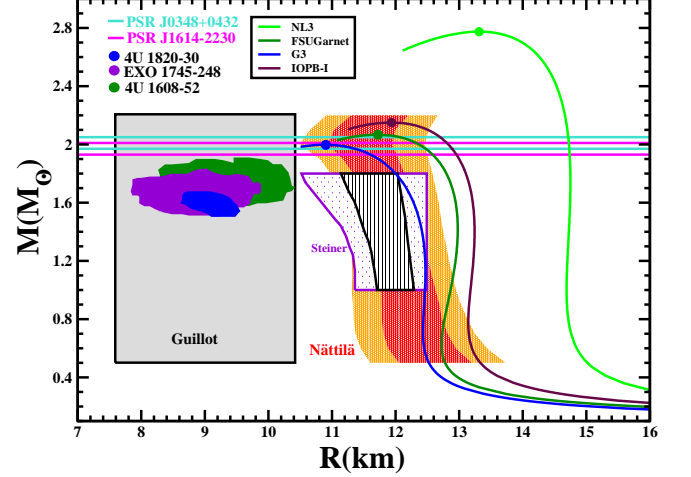


FIG. 7: (color online) The mass-radius profile predicted by NL3, FSUGarnet, G3 and IOPB-I. The recent observational constraints on neutron-star masses [101, 102] and radii [96, 97, 107, 108] are also shown.

and 461.03 of the $1.4 M_\odot$ NS binary for the IOPB-I, FSUGarnet and G3 parameter sets, respectively (see Tables IV and V). We also find a reasonably good agreement in the $\tilde{\Lambda}$ value equal to 582.26 for $1.35 M_\odot$ in the G3 EoS, which is obtained using a Markov Chain Monte Carlo simulation of BNS with $\tilde{\Lambda} \approx 600$ at signal-to-noise ratio of 30 in a single aLIGO detector [105, 106]. Finally, we close this section with the discussion on chirp mass \mathcal{M}_c and chirp radius \mathcal{R}_c of the BNS system which are defined as:

$$\mathcal{M}_c = (m_1 m_2)^{3/5} (m_1 + m_2)^{-1/5} \quad (50)$$

$$\mathcal{R}_c = 2 \mathcal{M}_c \tilde{\Lambda}^{1/5}. \quad (51)$$

The precise mass measurements of the NSs have been reported in Refs. [101, 102]. However, till now no observation has been confirmed regarding the radius of the most massive NS. Recently, aLIGO/VIRGO has measured chirp mass $1.188^{+0.004}_{-0.002} M_\odot$ with very good precision. With the help of this, we can easily calculate the chirp radius \mathcal{R}_c of the BNS system and we find that the chirp radius is in the range between $7.867 \leq \mathcal{R}_c \leq 10.350$ km for equal and unequal-mass BNS system as shown in Tables IV and V.

V. SUMMARY AND CONCLUSIONS

We built a new relativistic effective interaction for finite nuclei, infinite nuclear matter and neutron stars. The optimization has been done with experimental data of eight spherical nuclei such as binding energy and charge radius. The calculation is also comprised few constraints of the infinite nuclear matter data. The prediction of observables such as binding energies and radii with the new IOPB-I set for finite nuclei are quite good. The Z=120 isotopic chain shows that

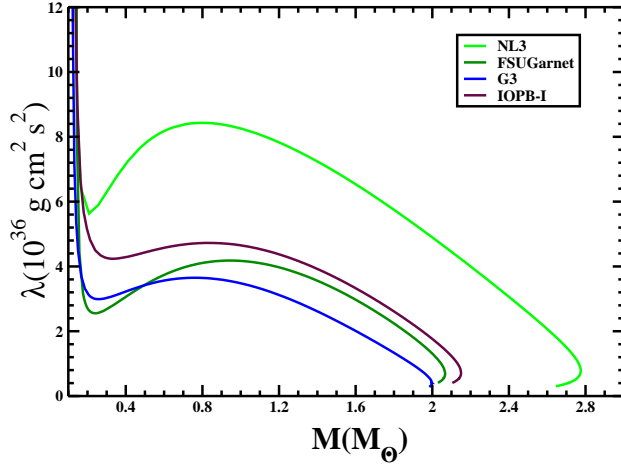


FIG. 8: (color online) The tidal deformability λ as a function of neutron star mass with different EoSs.

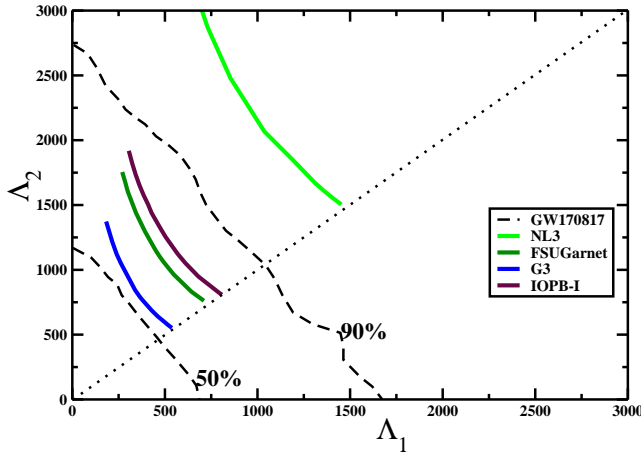


FIG. 9: (color online) Different values of Λ generated by using IOPB-I along with NL3, FSUGarnet and G3 EoSs are compared with the 90% and 50% probability contour in case of low-spin $|\chi| \leq 0.05$ as given in Fig. 5 of GW170817 [27].

the magicity appears at neutron numbers $N=172, 184,$ and 198 . Furthermore, we find that the IOPB-I set slightly overestimates the NST data. This is due to the small strength of the $\omega - \rho$ cross-coupling. For infinite nuclear matter at sub-saturation and supra-saturation densities, the results of our calculations match well with the known experimental data. The nuclear matter properties obtained by this new parameter set are listed as nuclear incompressibility $K = 222.65$ MeV, symmetry energy coefficient $J = 33.30$ MeV, symmetry energy slope $L = 63.58$ MeV, and the asymmetry term of nuclear incompressibility $K_\tau = 389.46$ MeV at saturation density $\rho_0 = 0.149 \text{ fm}^{-3}$. In general, all these values are consistent with current experimental data. The IOPB-I model satisfies the density dependence symmetry energy which are obtained from the different sets of experimental data. It also yields the NS maximum mass to be $2.15M_\odot$ which is consistent with the current GW170817 observational [103]. The radius of the canonical neutron star is 13.242 km compatible with the theoretical results in Ref. [98]. Similarly, the predicted values of dimensionless tidal deformabilities are in accordance with the GW170817 observational probability contour [27].

Our results will be very much useful for the the future planned experiments. The inclusion of isovector channel in the calculations and the fitting of the parameters both in sub-saturation and supra-saturation densities controls the vital constraints in the nuclear matter properties. The naturalness of the coupling constants are also taken during the fitting to keep the higher order contributions in order.

Acknowledgments: Bharat Kumar would like to take this opportunity to convey special thanks to P. Landry and Joonas Nättilä, fruitful discussions, and useful suggestions.

-
- [1] R. J. Furnstahl, B. D. Serot and H. B. Tang, Nucl. Phys. A **598**, 539 (1996); R. J. Furnstahl, B. D. Serot and H. B. Tang, Nucl. Phys. A **615**, 441 (1997).
 - [2] P. Arumugam, B. K. Sharma, P. K. Sahu, S. K. Patra, Tapas Sil, M. Centelles, and X. Viñas, Phys. Lett. B **601**, 51 (2004).
 - [3] M. Del Estal, M. Centelles, X. Viñas and S. K. Patra, Phys. Rev. C **63**, 024314 (2001).
 - [4] E. Chabanat, P. Bonche, P. Haensel, J. Meyer, and R. Schaeffer, Nucl. Phys. A **635**, 231 (1998).
 - [5] N. Sandulescu, Nguyen Van Giai, and R. J. Liotta, Phys. Rev. C **61**, 061301(R) (2000).
 - [6] J. Dobaczewski, H. Flocard, and J. Treiner, Nucl. Phys. A **422**, 103 (1984).
 - [7] J. Dobaczewski, W. Nazarewicz, T. R. Werner, J. F. Berger, R. C. Chin, and J. Decharge, Phys. Rev. C **53**, 2809 (1996).
 - [8] J. Decharge and D. Gogny, Phys. Rev. C **21**, 1568 (1980).
 - [9] J. D. Walecka, Ann. Phys. (N. Y.) **83**, 491 (1974).
 - [10] J. Boguta and A. R. Bodmer, Nucl. Phys. A **292**, 413 (1977).
 - [11] P.-G. Reinhard, Rep. Prog. Phys. **52**, 439 (1989).
 - [12] M. M. Sharma, G. A. Lalazissis and P. Ring, Phys. Lett. B **317**, 103 (1993).

- 9 (1993).
- [13] G. A. Lalazissis, J. König and P. Ring, Phys. Rev. C **55**, 540 (1997).
- [14] G. A. Lalazissis, S. Karatzikos, R. Fossion, D. Pena Arteaga, A. V. Afanasjev and P. Ring, Phys. Lett. B **671**, 36 (2009).
- [15] A. R. Bodmer, Nucl. Phys. A **526**, 703 (1991)
- [16] S. Gmuca, Nucl. Phys. A **547**, 447 (1992); J. K. Bunta and S. Gmuca, Phys. Rev. C **68**, 054318 (2003).
- [17] Y. Sugahara and H. Toki, Nucl. Phys. A **579**, 557 (1994).
- [18] D. Vretenar, G. A. Lalazissis and P. Ring, Phys. Rev. C **62**, 045502 (2000).
- [19] B. G. Todd-Rutel and J. Piekarewicz, Phys. Rev. Lett **95**, 122501 (2005); C. J. Horowitz and J. Piekarewicz, Phys. Rev. Lett. **86**, 5647 (2001); Phys. Rev. C **64**, 062802 (R) (2001).
- [20] S. Kubis and M. Kutschera, Phys. Lett. B **399**, 191 (1997).
- [21] Bharat Kumar, S. K. Singh, B. K. Agrawal, S. K. Patra Nucl. Phys. A **966**, 197 (2017).
- [22] G. Ferini, M. Colonna, T. Gaitanos and M. Di Toro, Nucl. Phys. A **762**, 147 (2005).
- [23] H. Chiu and E. E. Salpeter, Phys. Rev. Lett. **12**, 413 (1964).
- [24] J. N. Bahcall and R. A. Wolf, Phys. Rev. Lett. **14**, 343 (1965).
- [25] J. M. Lattimer, C. J. Pethic, M. Prakash and P. Haensel, Phys. Rev. Lett. **66**, 2701 (1991).
- [26] C. J. Horowitz, S. J. Pollock, P. A. Souder and R. Michaels, Phys. Rev. C **63**, 025501 (2001).
- [27] P. B. Abbott *et al.*, Phys. Rev. Lett. **119**, 161101 (2017).
- [28] É.É. Flanagan and T. Hinderer, Phys. Rev. D **77**, 021502 (2008).
- [29] T. Hinderer, Astrophys. J. **677**, 1216 (2008); 697964(E) (2009).
- [30] T. Hinderer, B. D. Lackey, R. N. Lang, and J. S. Read, Phys. Rev. D **81**, 123016 (2010).
- [31] J. M. Lattimer and M. Prakash, Phys. Rept. **442**, 109 (2007).
- [32] Bharat Kumar, S. K. Biswal and S. K. Patra, Phys. Rev. C **95**, 015801 (2017).
- [33] B. K. Agrawal, S. Shlomo and V. K. Au, Phys. Rev. C **72**, 014310 (2005).
- [34] B. K. Agrawal, Shashi K. Dhiman and Raj Kumar, Phys. Rev. C **73**, 034319 (2006).
- [35] Raj Kumar, B. K. Agrawal and Shashi K. Dhiman, Phys. Rev. C **74**, 034323 (2006).
- [36] H. Müller and B. D. Serot, Nucl. Phys. A **606**, 508 (1996).
- [37] B. D. Serot and J. D. Walecka, Int. J. Mod. Phys. E **6**, 515 (1997).
- [38] S. K. Singh, S. K. Biswal, M. Bhuyan, S. K. Patra, Phys. Rev. C **89**, 044001 (2014).
- [39] J. P. Elliott and T. H. R. Skyrme, Proc. Soc. (London) A **232**, 561 (1955).
- [40] J. W. Negele Phys. Rev. C **1**, 1260 (1970).
- [41] B. D. Serot and J. D. Walecka, Adv. Nucl. Phys. **16**, 1 (1986).
- [42] W. Kohn and L. J. Sham, Phys. Rev. A **140**, 1133 (1965); C. Speicher, R. M. Dreizler, and E. Engel, Ann. Phys. N.Y. **213**, 312 (1992).
- [43] T. Matsui, Nucl. Phys. A **370**, 365 (1981).
- [44] X. Roca-Maza, X. Viñas, M. Centelles, P. Ring and P. Schuck, Phys. Rev. C **84**, 054309 (2011).
- [45] S. K. Singh, M. Bhuyan, P. K. Panda and S. K. Patra, J. Phys. G: Nucl. Part. Phys. **40**, 085104 (2013).
- [46] C. J. Horowitz and J. Piekarewicz, Phys. Rev. C **64**, 062802 (R) (2001).
- [47] L. -W. Lattimer, B. -J. Cai, C. M. Ko, B. -A. Li, C. Shen and J. Xu, Phys. Rev. C **80**, 014322 (2009).
- [48] M. B. Tsang *et al.*, Phys. Rev. C **86**, 15803 (2012).
- [49] M. Dutra *et al.*, Phys. Rev. C **85**, 035201 (2012).
- [50] C. Xu, B.-A. Li and L.-W. Chen, Phys. Rev. C **82**, 054607 (2010).
- [51] W. G. Newton, M. Gearheart and B.-A. Li, arXiv:1110.4043.
- [52] A. W. Steiner and S. Gandolfi, Phys. Rev. Lett. **108**, 081102 (2012).
- [53] F. J. Fattoyev, W. G. Newton, J. Xu and B.-A. Li, Phys. Rev. C **86**, 025804 (2012).
- [54] M. Centelles, X. Roca-Maza, X. Viñas and M. Warda, Phys. Rev. Lett. **102**, 122502 (2009).
- [55] B. A. Li and X. Han, Phys. Lett. B **727**, 276 (2013).
- [56] S. Kirkpatrick, C. D. Gelatt and M. P. Vecchi, Science **220**, 671 (1983).
- [57] W. H. Press, S. A. Teukolsky, W. T. Vetterling and B. P. Flannery, Numerical Recipes in Fortran, (Cambridge University Press, New York, 1992).
- [58] S. Kirkpatrick, J. Stat. Phys. **34**, 975 (1984).
- [59] L. Ingber, Math. Comput. Model. **12**, 967 (1989).
- [60] B. Cohen, Masters thesis, Tel-Aviv University, 1994.
- [61] Wei-Chai Chen and J. Piekarewicz, Phys. Lett. B **748**, 284 (2015).
- [62] M. Wang, G. Audi, A. H. Wapstra, F. G. Kondev, M. MacCormick, X. Xu and B. Pfeiffer, Chin. Phys. C **36**, 1603 (2012).
- [63] I. Angeli, K. P. Marinova, At. Data and Nucl. Data Tables **99**, 69 (2013).
- [64] S. K. Patra, Int. J. Mod. Phys. E **2**, 471 (1993).
- [65] R. F. Garcia Ruiz *et al.*, Nature Phys. **12**, 594 (2016).
- [66] B. A. Brown, Phys. Rev. Lett. **85**, 5296 (2000).
- [67] P. G. Reinhard and W. Nazarewicz, Phys. Rev. C **81**, 051303 (R) (2010).
- [68] X. Roca-Maza, M. Centelles, X. Viñas, and M. Warda, Phys. Rev. Lett. **106**, 252501 (2011).
- [69] A. Trzcińska, J. Jastrzebski, P. Lubiński, F. J. Hartmann, R. Schmidt, T. von Egidy, and B. Klos, Phys. Rev. Lett. **87**, 082501 (2001); J. Jastrzebski, A. Trzcińska, P. Lubiński, B. Klos, F. J. Hartmann, T. von Egidy, S. Wycech, Int. J. Mod. Phys. E **13** (2004) 343.
- [70] P. Möller, A. J. Sierk, T. Ichikawa, and H. Sagawa, At. Data Nucl. Data Tables **109**, 1 (2016).
- [71] X. Viñas, M. Centelles, X. Roca-Maza and M. Warda, Eur. Phys. J. A **50** (2014) 27.
- [72] J. Zenihiro *et al.*, Phys. Rev. C **82**, 044611 (2010).
- [73] A. T. Gallant *et al.*, Phys. Rev. Lett. **109**, 032506 (2012).
- [74] K. Rutz, M. Bender, T. Bürvenich, T. Schilling, P. -G. Reinhard, J. A. Maruhn and W. Greiner, Phys. Rev. C **56**, 238 (1997); M. Bhuyan and S. K. Patra, Mod. Phys. Lett. A **27**, 1250173 (2012).
- [75] R. K. Gupta, S. K. Patra and W. Greiner, Mod. Phys. Lett. A **12**, 1727 (1997).
- [76] S. K. Patra, C. -L. Wu, C. R. Praharaaj and R. K. Gupta, Nucl. Phys. A **651**, 117 (1999).
- [77] M. S. Mehta, Harvinder Kaur, Bharat Kumar, and S. K. Patra, Phys. Rev. C **92**, 054305 (2015).
- [78] G. Coló, U. Garg, and H. Sagawa, Eur. Phys. J. A **50**, 26 (2014).
- [79] J. Piekarewicz, Eur. Phys. J. A **50**, 25 (2014).
- [80] P. Danielewicz and J. Lee, Nucl. Phys. A **922**, 1 (2014).
- [81] M. B. Tsang, Y. Zhang, P. Danielewicz, M. Famiano, Z. Li, W. G. Lynch, and A. W. Steiner, Phys. Rev. Lett. **102**, 122701 (2009); Int. J. Mod. Phys. E **19**, 1631 (2010).
- [82] P. Russotto *et al.*, Phys. Rev. C **94**, 034608 (2016).
- [83] C. Mondal, B. K. Agrawal, M. Centelles, G. Coló, X. Roca-Maza, N. Paar, X. Viñas, S. K. Singh, and S. K. Patra, Phys. Rev. C **93**, 064303 (2016).

- [84] J. R. Stone, N. J. Stone, and S. A. Moszkowski, *Phys. Rev. C* **89**, 044316 (2014).
- [85] J. M. Pearson, N. Chamel, and S. Goriely, *Phys. Rev. C* **82**, 037301 (2010).
- [86] T. Li *et al.*, *Phys. Rev. C* **81**, 034309 (2010).
- [87] U. Garg *et al.*, *Nucl. Phys. A* **788**, 36 (2007).
- [88] B. Friedman and V. R. Pandharipande, *Nucl. Phys. A* **361**, 502 (1981).
- [89] C. Mondal, B. K. Agrawal, J. N. De, and S. K. Samaddar *Phys. Rev. C* **93**, 044328 (2016).
- [90] M. Baldo and C. Maieron, *Phys. Rev. C* **77**, 015801 (2008).
- [91] S. Gandolfi, A. Yu. Illarionov, S. Fantoni, F. Pederiva, and K. E. Schmidt, *Phys. Rev. Lett.* **101**, 132501 (2008).
- [92] A. Gezerlis and J. Carlson, *Phys. Rev. C* **81**, 025803 (2010).
- [93] K. Hebeler, J. M. Lattimer, C. J. Pethick and A. Schwenk, *Astrophys. J.* **773**, 11 (2013).
- [94] P. Danielewicz, R. Lacey, and W. G. Lynch, *Science* **298**, 1592 (2002).
- [95] M. Praksh, T. L. Ainsworth and J. M. Lattimer, *Phys. Rev. Lett.* **61**, 2518 (1988).
- [96] J. Nättälä, A. W. Steiner, J. J. E. Kajava, V. F. Suleimanov and J. Poutanen, *A. & A.* **591**, 25 (2016).
- [97] A. W. Steiner, J. M. Lattimer and E. F. Brown, *Astrophys. J.* **722**, 33 (2010).
- [98] Eemeli Annala, Tyler Gorda, Aleks Kurkela and Aleks Vuorinen, arXiv:1711.02644v1.
- [99] P. Landry and Eric Poisson, *Phys. Rev. D* **89**, 124011 (2014).
- [100] J. R. Oppenheimer and G. M. Volkoff, *Phys. Rev.* **55**, 374 (1939); R. C. Tolman, *ibid.* **55**, 364 (1939).
- [101] P. B. Demorest, T. Pennucci, S. M. Ransom, M. S. E. Roberts, and J. W. T. Hessels, *Nature (London)* **467**, 1081 (2010).
- [102] J. Antoniadis *et al.*, *Science* **340**, 6131 (2013).
- [103] L. Rezzolla, Elias R. Most and Lukas R. Weth, arXiv:1711.00314v1.
- [104] A. W. Steiner, S. Gandolfi, F. J. Fattoyev, and W. G. Newton, *Phys. Rev. C* **91**, 015804 (2015).
- [105] M. Favata, *Phys. Rev. Lett.* **112**, 101101 (2014).
- [106] L. Wade, J. D. E. Creighton, E. Ochsner, B. D. Lackey, B. F. Farr, T. B. Littenberg, and V. Raymond, *Phys. Rev. D* **89**, 103012 (2014).
- [107] F. Ozel, G. Baym and T. Guver, *Phys. Rev. D* **82**, 101301 (2010).
- [108] V. Suleimanov, J. Poutanen, M. Revnivtsev and K. Werner, *Astrophys. J.* **742**, 122 (2011).
- [109] P. B. Abbott *et al.*, arXiv:1710.09320v1.
- [110] D. Radice, A. Perego and F. Zappa, arXiv:1711.03647v1.